Characterising the maximal invariant set of a map with (robust) heterodimensional cycles

Sam Doak, Bernd Krauskopf and Hinke M. Osinga

Department of Mathematics, The University of Auckland
Private Bag 92019, Auckland 1142, New Zealand

1 September 2026

Abstract

We present a case study of a three-dimensional diffeomorphism called the shear rotation map T. This one-parameter map has been proposed as the first example of an explicitly given discrete-time dynamical system that potentially has *heterodimensional cycles*. A heterodimensional cycle consists of two heteroclinic orbits between saddle periodic points of different index (number of unstable eigenvalues). In the (minimal) three-dimensional case considered here, one heteroclinic orbit lies in the non-transverse intersection of a one-dimensional stable and one-dimensional unstable manifold, and the other in the transverse intersection of the corresponding two-dimensional manifolds. Our goal is to characterize the bounded maximal invariant set Λ of T for a fixed parameter value. To this end, we design an efficient algorithm to compute millions of periodic orbits in Λ, and find that those with one-dimensional unstable manifolds are densely intermingled with those that have one-dimensional stable manifolds. Hence, Λ cannot be a hyperbolic set. We then focus on and compute to long arclengths the one-dimensional unstable and stable manifolds of the two fixed points of T and show that they have the so-called *carpet property* of 'behaving like a surface'; this strongly suggests that T has robust heterodimensional cycles. Subsequently, we define suitably formulated boundary-value problems to find both a non-transverse heteroclinic orbit and a one-dimensional family of transverse return orbits between the two fixed points. This is the first heterodimensional cycle computed for an explicit diffeomorphism. Our case study of the properties of the invariant set Λ of T is representative in that it demonstrates generic properties of diffeomorphisms with robust heteterodimensional cycles — the key objects used to prove that nonhyperbolic dynamics can be persistent in open sets of diffeomorphisms.

1 Introduction

When modeling a real-world phenomenon as a dynamical system, small errors are often introduced, for example, through simplifying assumptions. Nevertheless, the model still describes the phenomenon of interest if its qualitative behavior is structurally stable; that is, it persists under sufficiently small perturbations [21, 35, 41]. In this paper, we focus on *discrete-time* dynamical systems given by a diffeomorphism, that is, a smooth map with a smooth inverse [9, 15, 29, 39]. The persistence of the qualitative behavior of such a system requires that any fixed or periodic points are hyperbolic with stable and unstable manifolds that intersect transversely, if at all [34, 37, 38]. In the mid 1960s, it was widely believed that systems with this property are typical, in the sense that loss of hyperbolicity or non-transverse intersections are not robust phenomena [3, 40]. However, in 1970, Abraham and Smale [1] constructed an open set of four-dimensional diffeomorphisms that all have non-transverse intersections of stable and unstable manifolds. This showed that there are open sets of diffeomorphisms that are not structurally stable.

The construction in [1] relied on the presence of a *heterodimensional cycle*, which is a pair of heteroclinic orbits connecting two saddle fixed or periodic orbits with unstable manifolds of different dimension [7, 16, 18, 31]; this dimension is referred to as the *index* of the saddle orbit. For example, in dimension three (the minimum dimension required), the one-dimensional unstable manifold of an index-one saddle and the one-dimensional stable manifold of an index-two saddle intersect in a heteroclinic orbit and, simultaneously, the stable and unstable two-dimensional manifolds of the two points intersect in a one-dimensional family of transverse return connecting orbits. Note that the two one-dimensional manifold must necessarily intersect non-transversely in the three-dimensional phase space; hence, the corresponding connecting orbit is not a robust object, which seemingly provides a contradiction with the result in [1] and the more recent literature on the robust occurrence of heterodimensional cycles [7, 16, 18, 31].

In spite of the importance of heterodimensional cycles for recent developments of the theory, there are hardly any examples of explicitly given dynamical systems that are known to feature them. To our knowledge, only the so-called Atri model, a four-dimensional vector field, is known to have a heterodimensional cycle between two periodic orbits, which has been found numerically with a boundary-value problem formulation [43]. This example can be viewed as a discrete-time system defined by the return map to a three-dimensional Poincaré section, which then has a heterodimensional cycle between two fixed points of different index [23], as described above. A subsequent bifurcation study of the Atri model discovered many more heterodimensional cycles of different types [42]. We do not know any example of a diffeomorphism for which a heterodimensional cycle has been computed explicitly. However, a candidate diffeomorphism designed to exhibit heterodimensional cycles was recently introduced in [22, 32]. The underlying map, which we call the *shear-rotation map*, has its origins in multi-parameter models of particle accelerators [24, 33], but in [32], it is defined in the form of a diffeomorphism that depends on only one parameter $k \in \mathbb{R}$ as follows:

$$\begin{array}{rccl} T: & \mathbb{R}^3 & \to & \mathbb{R}^3 \\ & (x,y,z) & \mapsto & (z + k(x^2+y^2-2), x, y). \end{array} \tag{1}$$

The map T was studied in [32] for the fixed parameter value $k = \sqrt{20}$. This project focused on finding the maximal invariant set Λ, which is the set of all orbits of T that remain bounded in both forward and backward time; see Definition 1 for a precise definition. In [32], Λ is referred to as the chain recurrent set [13], which is approximated numerically by the box-covering algorithm implemented in the software package `GAIO` [14]. The dissertation [32] also reports on using `GAIO` to compute periodic orbits in Λ for periods up to 11, as well as their one-dimensional stable or unstable manifolds, which were computed by iterating points in the corresponding stable or unstable eigenspaces. The map T has two hyperbolic fixed points, which we call p^+ and p^-, and a first part the two-dimensional stable and unstable manifolds of these two fixed points were computed with `GAIO` in [32] as well.

In this paper, we build upon the results from [32] and perform a comprehensive investigation of the global dynamics of T when $k = \sqrt{20}$. To set the stage, Fig. 1 presents a global phase portrait of T for $k = \sqrt{20}$; where the phase space $\mathbb{R}^3$ has been compactified to the unit ball $\mathbb{B}^3$; see Section 2 for details of this compactification. Fig. 1 shows over 18 million periodic orbits of T, with periods up to 26, that have been computed with the algorithm described in Section 3. These periodic orbits all lie in the maximal invariant set Λ and, together, they form a good approximation of Λ. The one-dimensional invariant manifolds $W^u(p^+)$ and $W^s(p^-)$ of the two fixed points p^+ and p^-, which have index one and two, respectively, are shown in Fig. 1 as well. Both were computed as curves with the method in [11] up to an arclength of $L = 1{,}500$ as measured in compactified coordinates, and they are shown with a color gradient that lightens as the arclength increases. Observe that $W^u(p^+)$ and $W^s(p^-)$ make long excursions towards the boundary of $\mathbb{B}^3$; more specifically, $W^u(p^+)$ repeatedly approaches the point $(1, 0, 0)$ and, similarly, $W^s(p^-)$ approaches $(0, 0, -1)$; these excursions represent positive and negative infinity along the x and z-axes, respectively. In between them, both $W^u(p^+)$ and $W^s(p^-)$ form a thick 'weaving' that appears to 'fill out' a surface; indeed, already for $L = 1500$, both $p^\pm$ are obscured from view in Fig. 1. The figure suggests that $W^u(p^+)$ and $W^s(p^-)$ intersect and there exists a heterodimensional

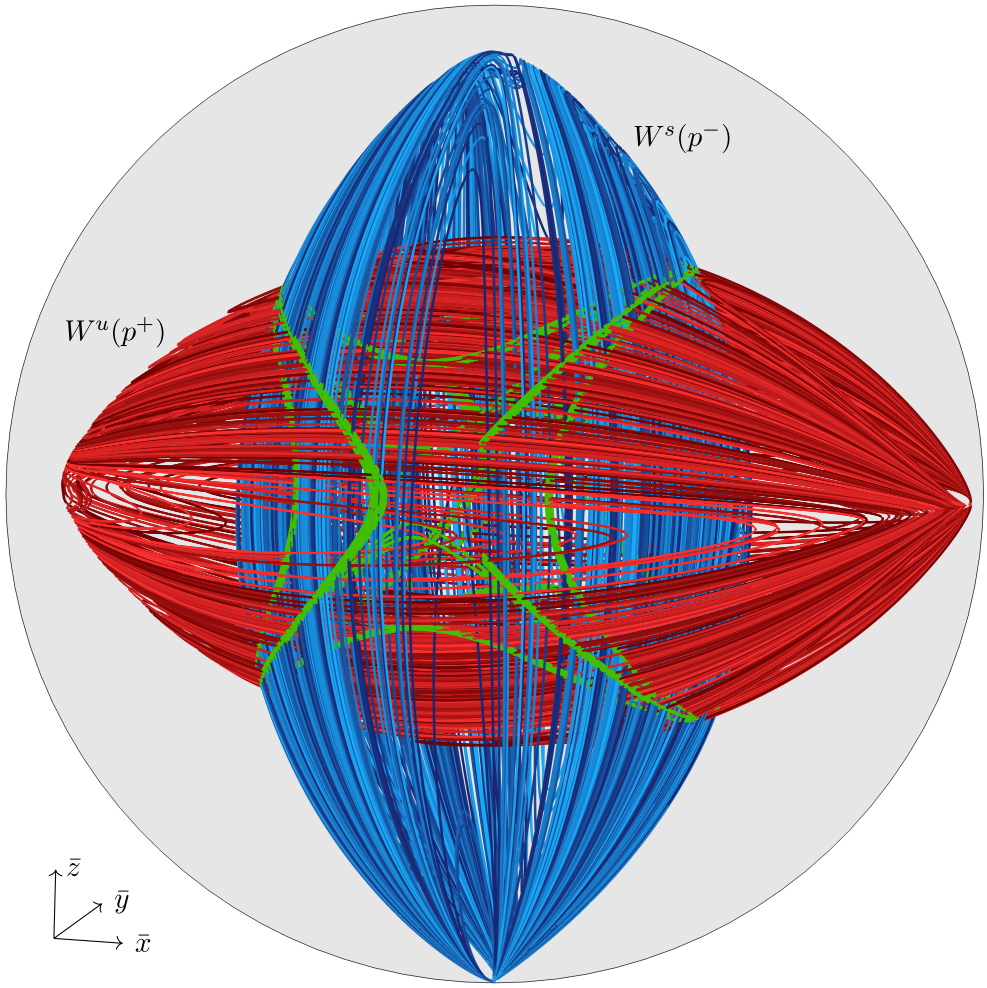

Figure 1: Phase portrait of T for $k = \sqrt{20}$ in the compactified phase space $\mathbb{B}^3$ (gray sphere). Shown are the one-dimensional manifolds $W^u(p^+)$ (red curve) and $W^s(p^-)$ (blue curve) of the fixed points $p^\pm$ up to an arclength of $L = 1{,}500$, colored in a gradient that lightens as arclength increases. Also shown is the maximal invariant set Λ approximated by all periodic points up to period 26 (green dots). See also the accompanying animation (dko_hetdim_anim_fig01.mp4 [3.7MB]).

cycle between p^+ and p^-.

As mentioned earlier, a possible intersection between the two one-dimensional manifolds $W^u(p^+)$ and $W^s(p^-)$ will be non-transverse, such that the existence of a specific heterodimensional cycle is not expected to be robust. The literature describes the most common way how one can transform a system with a single heterodimensional cycle into a system with robust heterodimensional cycles: the idea is to embed one of the fixed or periodic orbits of the heterodimensional cycle within a more complicated invariant set known as a *blender* [5, 6]. In three dimensions, a blender is a hyperbolic transitive set with a one-dimensional stable or unstable manifold that behaves like a surface in the sense that it cannot avoid intersections with a C^1-open family of curves. Consequently, the one-dimensional invariant manifold of the blender can have persistent non-transverse intersections with the one-dimensional manifold of another periodic orbit, leading to the robust existence of heterodimensional cycles [7].

We already know that T has the maximal invariant set Λ. Fig. 1 gives an impression of the overall shape of Λ, because we are able to find sufficiently many periodic orbits. However, the periodic points in Λ are evenly split into two sets of periodic orbits with the same index. Furthermore, the closure of either set separately yields the overall set Λ. Therefore, the two sets of index-one and -two periodic orbits are intermingled, which means, in particular, that Λ is not hyperbolic. In fact, this intermingling of points of different indices is very similar to what was found in [16] as a different approach to creating robust heterodimensional cycles.

While we characterize Λ as a complicated non-hyperbolic, intermingled invariant set, each point in Λ has well-defined one-dimensional (strong) unstable and (strong) stable manifolds. Fig. 1 suggests that, as the arclenths of the one-dimensional manifolds $W^u(p^+)$ and $W^s(p^-)$ increases, $W^u(p^+)$ and $W^s(p^-)$ become so dense that their closures act like surfaces. We refer to this characterizing property as the *carpet property* [12, 26, 27]; see Section 2 for more details. We use the method from [27] to verify this observation. More specifically, we compute $W^u(p^+)$ and $W^s(p^-)$ to very long arclengths and intersect them with a plane, where the surface-like property of the manifolds translates to a curve-like structure of the intersection points. By projecting the intersection points onto a one-dimensional submanifold, we demonstrate numerically that the closure of the projected points fills an open interval as the arclength is increased.

The surface-like properties of $W^u(p^+)$ and $W^s(p^-)$ suggest a non-empty intersection, at least for a nearby value of k. We present a method for finding a heteroclinic orbit in this intersection, as well as a return orbit to complete the heterodimensional cycle between p^+ and p^-. Specifically, we start from an approximate point of intersection and construct an associated pseudo-orbit with the method in [11]. The pseudo-orbit serves as a seed solution for a suitably defined boundary-value problem; corrections with Newton's method yield an accurate approximation of the corresponding non-transverse heteroclinic orbit, where k has changed only slightly from the value $k = \sqrt{20}$. The return heteroclinic orbit in the (transverse) intersection $W^u(p^-) \cap W^s(p^+)$ is found with a similar boundary-value problem setup for which k remains fixed; with pseudo-arclength continuation, we compute the one-dimensional family of return orbits for this value of k. We observe that both the non-transverse heteroclinic orbit and the curves in $W^u(p^-) \cap W^s(p^+)$ 'align' with the maximal invariant set Λ. Our results suggest that this represents the generic structure of a bounded maximal invariant set for a diffeomorphism with robust heterodimensional cycles.

This paper is organized as follows. We begin in Section 2 by describing the basic properties of the shear rotation map as well as introducing some of the relevant theory for heterodimensional cycles. In Section 3, we approximate Λ by the set of periodic orbits; we explain how we are able to compute the millions of periodic obits shown in Fig. 1. Section 4 provides evidence that the closures of the two one-dimensional manifolds $W^u(p^+)$ and $W^s(p^-)$ are guaranteed to intersect in the three-dimensional phase space. Consequently, we find that $W^u(p^+)$ cannot avoid intersection with the closure of $W^s(p^-)$, and we compute a heterodimensional cycles for a nearby value of the parameter k in Section 5. We summarize our results in Section 6, and propose directions for future research. Finally, Appendix A describes our algorithm for the efficient computation of periodic points for T, as well as how we determine their index.

2 Background and setting

The shear rotation map (1) is constructed as the composition of the quadratic-shear $(x, y, z) \mapsto (x, y, z + k\,[x^2 + y^2 - 2])$ and the the cyclic permutation of $(x, y, z) \mapsto (z, x, y)$, which is equivalent to a rotation by $\frac{2\pi}{3}$ about the axis $(1, 1, 1)$. Given that both the shear and the rotation are volume preserving, T is volume preserving as well. Consequently, T cannot have global attractors or repellors. The inverse of T is given by

$$T^{-1}(x, y, z) = (y, z, x - k\,[y^2 + z^2 - 2]). \tag{2}$$

The map T has two fixed points and two period-three orbits that lie at the corners of a cube in $\mathbb{R}^3$, independent of k. We label the fixed points

$$p^+ = (1,1,1) \text{ and } p^- = (-1,-1,-1),$$

and the period-three orbits

$$\begin{array}{rclclc} q^+ & = & \{q_1^+, q_2^+, q_3^+\} & = & \{(\ \ 1,-1,-1), (-1,\ \ 1,-1), (-1,-1,\ \ 1)\} & \text{and} \\ q^- & = & \{q_1^-, q_2^-, q_3^-\} & = & \{(-1,\ \ 1,\ \ 1), (\ \ 1,-1,\ \ 1), (\ \ 1,\ \ 1,-1)\}. & \end{array}$$

For $k > 0$, the fixed point p^+ has index one, because the Jacobian matrix $DT(p^+)$ has one unstable eigenvalue (and two stable ones), while p^- has index two. Similarly, for $k > 1$, the period-three orbit q^+ has index two, while q^- has index one. Since $p^\pm$ are hyperbolic saddles, the Stable Manifold Theorem [36] guarantees that each point has smooth, immersed stable and unstable manifolds, denoted $W^s(p^\pm)$ and $W^u(p^\pm)$, comprising all points that converge to $p^\pm$ under T and T^{-1}, respectively. These manifolds are tangent to, and have the dimensions as the stable and unstable eigenspaces at $p^\pm$. In particular, $W^s(p^+)$ is two dimensional, $W^u(p^+)$ is one dimensional, and the reverse is the case for $W^s(p^-)$ and $W^u(p^-)$.

The map T also has many higher-period periodic points, the existence of which depends on k. We refer to the set of all periodic points of minimal period n as the set

$$\mathsf{Per}^n := \left\{ \boldsymbol{x} \in \mathbb{R} \mid T^n(\boldsymbol{x}) = \boldsymbol{x} \text{ and } T^i(\boldsymbol{x}) \neq \boldsymbol{x} \text{ for all } 1 \leq i < n \right\}.$$

In particular, Per^n does not contain any points with periods that are divisors of n. We already saw that $\mathsf{Per}^1 = \{p^\pm\}$ and $\mathsf{Per}^3 = \{q^\pm\}$. Moreover, T has no period-two or period-four orbits, that is, $\mathsf{Per}^2 = \mathsf{Per}^4 = \emptyset$. For $n \geq 5$, we find that the set Per^n is non-empty for $k = \sqrt{20}$. We refer to the total set of periodic points of T as Per, and it is given by the (disjoint) union

$$\mathsf{Per} = \bigcup_{i=1}^{\infty} \mathsf{Per}^n.$$

We further distinguish periodic points by their index and refer to the set of all index-one periodic points as Per_1, and the set of all index-two periodic points as Per_2.

The dynamical systems given by T is reversible: T is topologically conjugate to its inverse $T^{-1} = R \circ T \circ R^{-1}$ via the homeomorphism

$$R(x, y, z) = (-z, -y, -x). \tag{3}$$

Being reversible has two geometric consequences on the phase space. Firstly, the image of an index-one period-n point under R gives an index-two period-n point, and vice versa. Indeed, each of $p^\pm$ and $q^\pm$ are related by the reversibility; that is, $R(p^\pm) = p^\mp$ and $R(q^\pm) = q^\mp$. Secondly, the image of the stable manifold of a period-n point under R gives the unstable manifold of its R-conjugate period-n point and, likewise, for the image of an unstable manifold. In particular, the image of $W^u(p^+)$ under R is $W^s(p^-)$.

All of the orbits in Per are certainly bounded and, therefore, must lie in some maximal invariant set of T, which is formally defined as follows.

Definition 1 (Locally maximal invariant set [39]) *Let $B \subset \mathbb{R}^3$ be closed. The maximal T-invariant set Λ_B of B is given by*

$$\Lambda_B = \bigcap_{n \in \mathbb{Z}} T^n(B).$$

In [32], it is shown that, for $k > 2$, all bounded orbits of T lie in the box $(x, y, z) \in [-2, 2] \times [-2, 2] \times [-2, 2] =: [-2, 2]^3$. Hence, for $k > 2$, there exists a maximal invariant set $\Lambda \subseteq [-2, 2]^3$, independent of the closed subset B, that contains all bounded orbits of T. For $k = \sqrt{20}$, the set Λ is very complicated, and we clarify its properties in the next section. In particular, it allows for the existence of heterodimensional cycles.

Definition 2 (Heterodimensional cycles in $\mathbb{R}^3$ [16]) *Let $p_1, p_2 \in \mathbb{R}^3$ be hyperbolic fixed or periodic points with index one and index two, respectively. A heterodimensional cycle connecting p_1 and p_2 consists of two heteroclinic orbits: a non-transverse connecting orbit from p_1 to p_2 in $W^u(p_1) \cap W^s(p_2)$ and a transverse connecting orbit from p_2 to p_1 in $W^u(p_2) \cap W^s(p_1)$.*

While a single heterodimensional cycle is not robust, the presence of heterodimensional cycles can be made robust by replacing (at least) one of the connected saddle points with a more complicated transitive hyperbolic set called a *blender* [5, 7]. There are different types of blenders, each with its own definition. They all have in common that they are transitive sets which are uniformly hyperbolic, that is, the set has a consistent index throughout; and they have stable or unstable manifolds that behave as if their dimension is larger than suggested by their index [17]. The key geometric characterization can be phrased as the so-called *carpet property* [26]: the respective one-dimensional manifold of any saddle point in the hyperbolic set has a dense projection, so that, colloquially speaking, one cannot see through it. This denseness implies that the hyperbolic set is indeed a blender because the closure of the one-dimensional manifold of any point in the manifold is the one-dimensional manifold of the hyperbolic set. Moreover, this is an open condition, and any C^1-family of curves close to the projection direction will intersect the one-dimensional manifold of the blender, as required by the abstract definitions of blenders [6].

Since $p^\pm \in \Lambda$ have different index, the set Λ of T is, unfortunately, not uniformly hyperbolic and, thus, cannot be a blender. Nevertheless, we find that the one-dimensional $W^u(p^+)$ and $W^s(p^-)$ have the carpet property. We use this observation to construct heterodimensional cycles.

In order to check the carpet property, we compute very long pieces of manifolds. For this purpose, it will be useful to consider a coordinate transformation that compactifies $\mathbb{R}^3$ to the unit ball $\mathbb{B}^3$. We define the compactification

$$\mathcal{C}(x, y, z) = (\bar{x}, \bar{y}, \bar{z}) := \frac{(x, y, z)}{1 + \sqrt{1 + r^2}}, \tag{4}$$

where $r = \|(x, y, z)\|$. It has the inverse

$$\mathcal{C}^{-1}(\bar{x}, \bar{y}, \bar{z}) = \frac{2(\bar{x}, \bar{y}, \bar{z})}{1 - \bar{r}^2},$$

where $\bar{r} = \|(\bar{x}, \bar{y}, \bar{z})\|$. The compactified diffeomorphism $\mathcal{C} \circ T \circ \mathcal{C}^{-1} : \mathbb{B}^3 \to \mathbb{B}^3$ is conjugate to T and it is also reversible via the homeomorphism $\mathcal{C} \circ R$; throughout, we will refer to the compactified map as T as well.

3 The maximal invariant set as the closure of periodic points

By definition, the maximal invariant set Λ of T contains all bounded orbits. Hence, we may approximate Λ by computing many periodic orbits. To achieve this, we numerically solve for entire orbits, rather than individual periodic points. This allows us to compute millions of periodic orbits efficiently; see Appendix A for details. In particular, we can accurately determine the sets Per^n for $1 \leq n \leq 26$. In addition, we separate the points in Per^n by index. Finding this separation necessitates computing the spectrum of high-period periodic orbits, which is a numerically sensitive task that requires increased precision. We find that the set of period-n orbits with $n \leq 23$ is

Table 1: Overview of the effort involved in computing all period-n orbits with periods up to 26. From left to right, the columns show the period n, the total number of points in Per^n, the total number of periodic orbits in Per^n, the local growth rate $g_T^{(n)}$ as defined in (5), the time it took to compute Per^n, and the time it took to separate Per^n by index.

n	$\lvert\mathsf{Per}^n\rvert$	$\frac{1}{n}\lvert\mathsf{Per}^n\rvert$	$g_T^{(n)}$	time (s) for Per^n	Per^n separation time (s)
5	30	6	0.6931	0.0939	0.4705
6	24	4	0.5776	0.0923	0.4791
7	126	18	0.6931	0.0933	1.1722
8	64	8	0.5237	0.0882	0.6626
9	450	50	0.6808	0.0892	3.1900
10	280	28	0.5743	0.0953	2.5016
11	1,364	124	0.6563	0.0945	8.5135
12	936	78	0.5729	0.1294	6.3966
13	4,498	346	0.6471	0.1752	26.2539
14	3,948	282	0.5938	0.1794	24.5634
15	15,510	1,034	0.6434	0.2297	95.1199
16	13,696	856	0.5956	0.4102	84.2666
17	51,544	3,032	0.6382	0.7298	317.8184
18	47,088	2,616	0.5983	1.2866	288.0314
19	163,020	8,580	0.6317	2.4500	992.5330
20	159,920	7,996	0.5992	4.7658	988.9010
21	534,870	25,470	0.6281	10.3682	3,646.554
22	583,924	26,542	0.6036	20.5057	3,952.367
23	1,806,328	78,536	0.6264	44.7350	9,720.938
24	1,984,080	82,670	0.6042	89.3406	-
25	5,977,350	239,094	0.6241	203.7565	-
26	6,693,804	257,454	0.6045	423.1983	-

exactly divided in half, as expected from the reversibility symmetry of T (3). We remark that the computations are already very expensive which is why we did not compute the indices of periodic orbits with periods 24, 25, and 26. The number of periodic points grows exponentially with n. Table 1 shows that Per^n grows from 30 points in Per^5 to over six million in Per^{26}. The total number of points is shown in the second column and the total number of periodic orbits in the third column. The last two columns show the computation time to find them and separate them by index on a desktop computer, respectively. The fourth column shows the growth rate of the number of period-n orbits, defined as

$$g_T^{(n)} = \frac{1}{n} \log \sum_{d|n}^{n} \lvert\mathsf{Per}^d\rvert, \tag{5}$$

which we compute by including all periodic divisors of n; we refer again to Appendix A for more details.

Figure 2 shows the fixed points $p^{\pm}$ and period-three orbits $q^{\pm}$, which lie on the corners of a cube, together with all period-n orbits in Per^n of periods $5 \leq n \leq 26$. The disjoint union $\cup_{i=1}^{26}\mathsf{Per}^i$ contains about 18.043 million points, which are all shown in Fig. 2(a), where each period is indicated by the color bar. Moreover, periodic orbits with periods $n \leq 15$ are shown as thicker dots. We also show the set $\cup_{i=1}^{23}\mathsf{Per}^i$ separated by index, with all index-one orbits (light green) shown in panel (b1) and those with index two in panel (b2). Note that points of different periods are not distributed equally throughout Λ. In particular, the points of lower periods, including the thicker points of periods $n \leq 15$, tend to cluster around the cube's corners.

Figure 2(a) provides strong numerical evidence that the set $\cup_{i=1}^{26}\mathsf{Per}^i$ is sufficient to represent

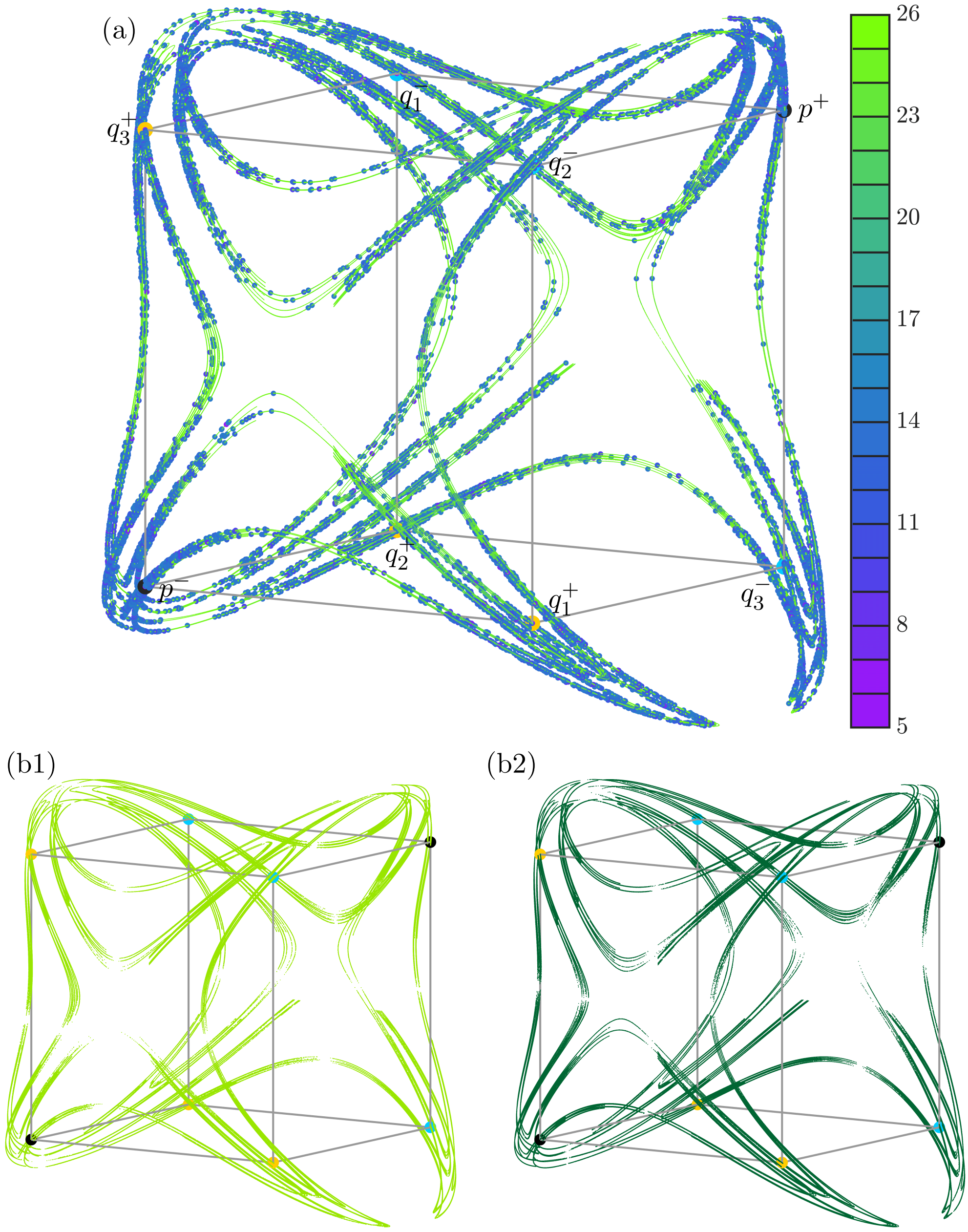

Figure 2: Periodic orbits of T_k for $k = \sqrt{20}$ with periods $n \leq 26$. All panels show the fixed (black) and period-three (yellow and blue) points, which lie at the corners of a cube (gray). The period-n orbits in $\cup_{i=5}^{26} \mathsf{Per}^i$ are shown with a color gradient in panel (a) as given by the color bar, and the dots for orbits with periods $n \leq 15$ are thicker. The period-n orbits with $n \leq 23$ are separated into those with index one (light green) and index two (dark green), shown in panels (b1) and (b2), respectively. See also the accompanying animation (dko_hetdim_anim_fig02.mp4 [2MB]).

the overall set of periodic points Per. Notice how the periodic points appear to align along curves. We conclude that the closure of Per is a complicated, seemingly connected set of curves of a fractal nature. We claim that $\cup_{i=1}^{26} \mathsf{Per}^i$ also provides a good approximation of the maximal invariant set Λ; this is consistent with the computation in [32, Figure 16] of Λ as the chain recurrent set [13], which is precisely what the software package `GAIO` [14] approximates.

Panels (b1) and (b2) of Fig. 2 show the subsets Per_1 and Per_2 as represented by the period-n points of index one and index two for $5 \leq n \leq 23$, respectively. Observe that, even though we

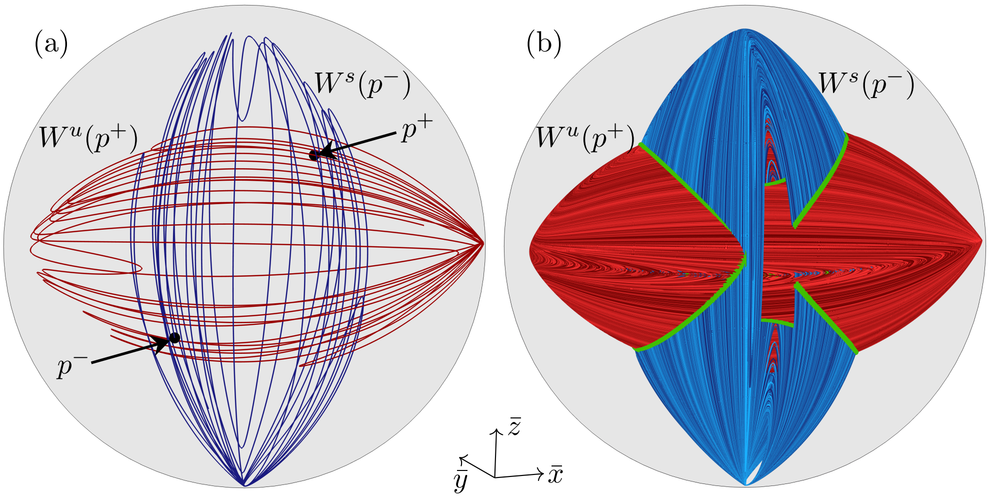

Figure 3: One branch of each the one-dimensional manifolds $W^u(p^+)$ (red) and $W^s(p^-)$ (blue) in $\mathbb{B}^3$, shown with a color gradient from darker to ligher with increasing arclength. Panel (a) shows the manifolds up to an arclength of $L = 60$, and panel (b) up to $L = 60{,}000$. Panel (b) also shows $\cup_{i=5}^{26}\mathsf{Per}^i$ (green dots); compare with Fig. 1, which is up to $L = 1{,}500$.

obtained neither set as the symmetric image of the other, panels (b1) and (b2), nevertheless, have the reversibility symmetry given by (3). Comparison of panels (b1) and (b2) with panel (a) shows that, separately, these index-one and index-two points take on practically the same shape as Λ. However, some of the curves in panel (a) are not as well approximated in panels (b1) and (b2); for example, the index-one points have a gap near the middle of the cube edge connecting p^- and q_1^+ in panel (b1); likewise, due to the reversible symmetry, the index-two points are not quite as dense near the cube edge connecting p^+ and q_3^-. Despite these small local differences, panels (b1) and (b2) suggest that Λ is densely filled with periodic points of each index; that is, we have $\Lambda = \mathrm{cl}(\mathsf{Per}_1) = \mathrm{cl}(\mathsf{Per}_2)$.

4 Invariant manifolds and their carpet property

As we already mentioned in the discussion of Fig. 1, the one-dimensional manifolds $W^u(p^+)$ and $W^s(p^-)$ already look like surfaces for $L = 1{,}500$, that is, they appear to have the carpet property. Recall that $W^s(p^-)$ is the image of $W^u(p^+)$ under R. Hence, we only verify the carpet property for $W^{(}p^{+})$. To this end, we compute $W^u(p^+)$ to a much larger arclength in compactified coordinates $(\bar{x}, \bar{y}, \bar{z}) \in \mathbb{B}^3$. Fig. 3 shows $W^u(p^+)$ and $W^s(p^-)$ up to arclengths $L = 60$ in panel (a) and $L = 60{,}000$ in panel (b). As in Fig. 1, we use a color gradient that gradually lightens with increasing arclength along the manifolds. For the relatively short arclength in panel (a), it is clear that both $W^u(p^+)$ and $W^s(p^-)$ are curves. However, as their arclength increases, these manifolds accumulate so densely that they give the impression of surfaces in $\mathbb{B}^3$, resembling two ellipsoids. This is illustrated in Fig. 3(b), where we also plot the approximation $\cup_{i=5}^{26}\mathsf{Per}^i$ of Λ for reference.

To verify the visual evidence in Fig. 3, we employ the numerical test of the carpet property developed in [27]. Briefly, this test involves computing the intersection set of $W^u(p^+)$ or $W^s(p^-)$ with a planar section, and showing that the projection of these intersection points onto a one-dimensional submanifold becomes dense as the arclength grows. Specifically, we consider the planar section $\Sigma := \left\{(\bar{x}, \bar{y}, \bar{z}) \in \mathbb{B}^3 \mid \bar{x} = \bar{z}\right\}$, which contains $p^\pm$ and preserves the symmetry R from (3). This particular choice for Σ was made for convenience: this section is perpendicular to the axis of rotation of R and, thus, the intersection sets $\widehat{W}^u(p^+) := W^u(p^+) \cap \Sigma$ and

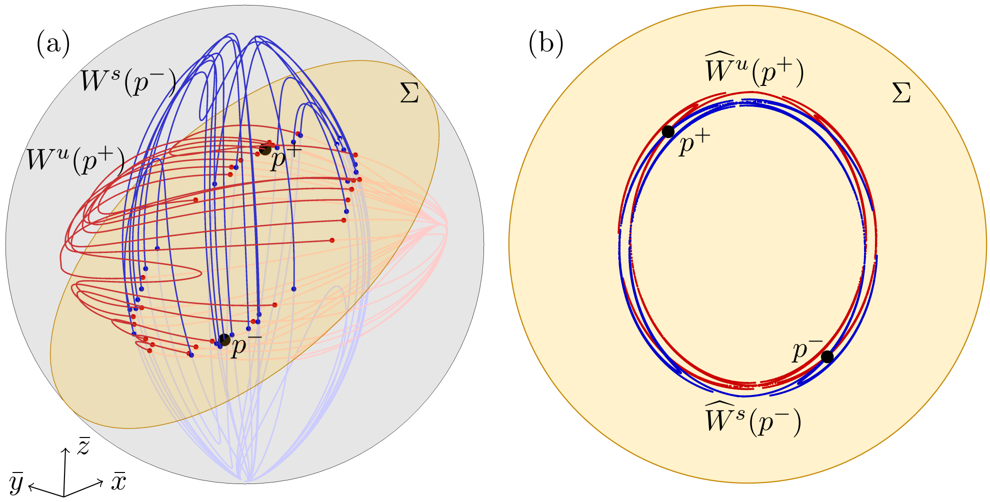

Figure 4: Intersections of $W^u(p^+)$ (red) and $W^s(p^-)$ (blue) with the plane $\Sigma := \{(\bar{x}, \bar{y}, \bar{z}) \in \mathbb{B}^3 \mid \bar{x} = \bar{z}\}$ (yellow). Panel (a) shows the situation in $\mathbb{B}^3$ with $W^u(p^+)$ and $W^s(p^-)$ up to $L = 60$. Panel (b) shows Σ with the 29,925 intersection points in each of $\widehat{W}^u(p^+) := W^u(p^+) \cap \Sigma$ and $\widehat{W}^s(p^-) := W^s(p^-) \cap \Sigma$, when each manifold is computed up to $L = 63{,}956$. Compare with Fig. 3.

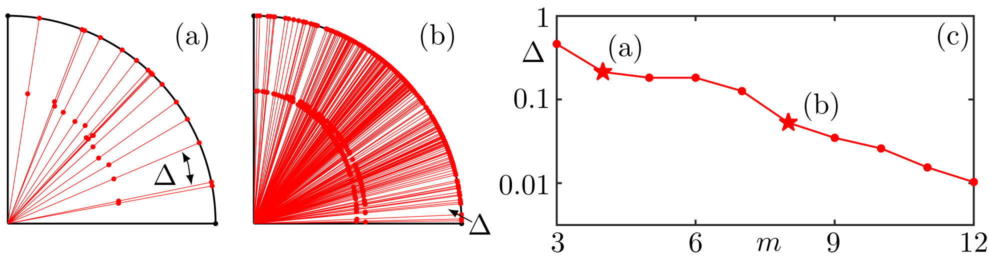

Figure 5: Checking the carpet property for $W^u(\boldsymbol{p}^+)$. Panels (a) and (b) show the radial projection of 2^4 and 2^8 intersection points in $\widehat{W}^u(\boldsymbol{p}^+)$ onto the upper-right quadrant of $\mathbb{S}^1$, respectively. These specific data points are highlighted by stars in panel (c), which displays the size Δ of the largest angular gap between points in $\widehat{W}^u(\boldsymbol{p}^+)$ in radians on a logarithmic scale against the power m of the first 2^m intersection points in $\widehat{W}^u(p^+)$.

$\widehat{W}^s(p^-) := W^s(p^-) \cap \Sigma$ are also R-conjugate; otherwise, any sufficiently transverse section would yield qualitatively the same intersection sets, which would then both need to be computed and no longer have the same rotational symmetry.

Figure 4 shows the intersection sets $\widehat{W}^u(p^+)$ and $\widehat{W}^s(p^-)$ in the compactified phase space in panel (a) and in the planar section Σ in panel (b). Panel (a) illustrates how the intersection points in $\widehat{W}^u(p^+)$ and $\widehat{W}^s(p^-)$ are created as the corresponding one-dimensional manifolds intersect Σ in $\mathbb{B}^3$. Here, $W^u(p^+)$ and $W^s(p^-)$ are only shown up to arclengths $L = 60$, and the segments that lie below Σ are shown in a fainter color shade; compare with Fig. 3(a). Panel (b) shows 29,925 intersection points in each of $\widehat{W}^u(p^+)$ and $\widehat{W}^s(p^-)$, obtained for the much larger arclength $L = 63{,}956$. Notice how the points in $\widehat{W}^u(p^+)$ and $\widehat{W}^s(p^-)$ appear to accumulate and align along 'layers' of curves that are almost circular. This 'curve-like' behavior of the intersection points in Σ is a manifestation of the 'surface-like' properties of the one-dimensional manifolds in $\mathbb{B}^3$.

Following [27], we now investigate whether $\widehat{W}^u(p^+)$ densely fills a projection onto a one-dimensional submanifold. Owing to the structure observed in Fig. 4, we consider the radial

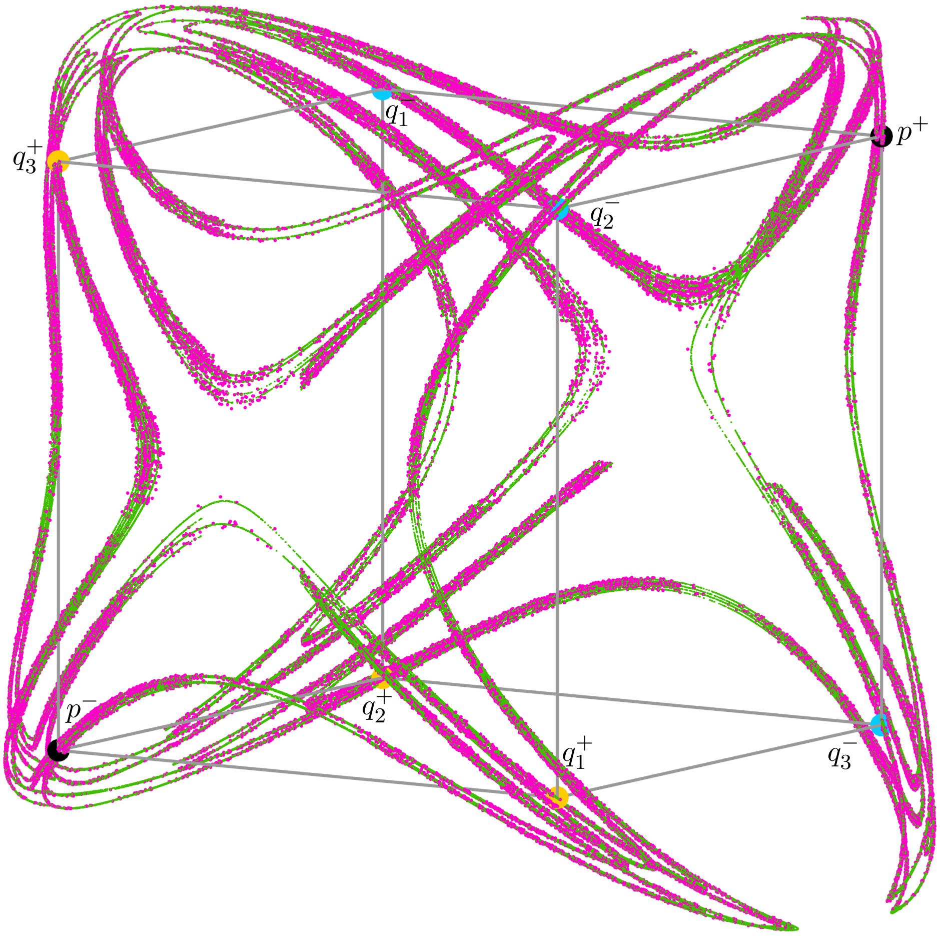

Figure 6: The averages Ψ_ε (magenta) in $\mathbb{R}^3$ of points $\boldsymbol{x}_u \in W^u(p^+)$ and $\boldsymbol{x}_s \in W^s(p^-)$, for which the difference in compactified coordinates satisfies $\|\boldsymbol{x}_u - \boldsymbol{x}_s\|_\infty < \varepsilon = 10^{-3}$. For comparison, we also plot the periodic points (green) up to period 26, as well as $p^\pm$ (black) and the period-three cycles $q^\pm$ (blue and yellow). See also the accompanying animation (dko_hetdim_anim_fig06.mp4 [2MB]).

projection of $\widehat{W}^u(p^+)$ onto S^1, where we restrict our attention to the top right quarter disk of Σ in $\mathbb{B}^3$. Panels (a) and (b) of Fig. 5 show this quarter disk with the first 2^m intersection points for $m = 4$ and $m = 8$, respectively, projected radially onto $\mathbb{S}^1$. The coordinates of the projected points are now given in radians; hence, we can order them by their angle and use this ordering to find the maximal angular gap Δ between adjacent intersection points. Panel (c) illustrates, on a logarithmic scale, that $\Delta = \Delta(m)$ decreases as we double the number of intersection points; the specific data points shown in panels (a) and (b) are highlighted with stars. Indeed, the maximal angular gap between the first $2^4 = 16$ intersection points in panel (a) is $\Delta \approx 0.2134$, but between the first $2^8 = 256$ points in panel (b) we already find $\Delta \approx 0.0528$. The decreasing linear trend in panel (c) suggests that $\Delta(m) \to 0$ as $m \to \infty$. We find that the size of $\Delta(m)$ reduces by a factor of approximately 0.66 when the number of intersection points doubles. Consequently, we conclude that $\widehat{W}^u(p^+)$ is dense in this projection and, therefore, $W^u(p^+)$ has the carpet property. By symmetry, the same analysis applies to $W^s(p^-)$.

5 Existence of heterodimensional cycles

Since $W^u(p^+)$ and $W^s(p^-)$ both have the carpet property, the closure either manifold cannot avoid being intersected by the other A heterodimensional cycle between p^+ and p^- consists of a non-transverse heteroclinic intersection of the one-dimensional manifolds $W^u(p^+)$ and $W^s(p^-)$ and a transverse (return) heteroclinic intersection of the respective two-dimensional manifolds. We begin with the problem of finding a non-transverse intersection — which is more difficult because its existence is not generic. Fig. 1 already strongly suggests that $W^u(p^+)$ and $W^s(p^-)$ may intersect, as the manifolds come very close to each other near the set of periodic points. We make this observation precise by identifying where the one-dimensional manifolds $W^u(p^+)$ and $W^s(p^-)$ are near each other. More specifically, we define the set

$$\Psi_\varepsilon := \left\{ \tfrac{1}{2}(\boldsymbol{x}_u + \boldsymbol{x}_s) \in \mathbb{B}^3 \mid \boldsymbol{x}_u \in W^u(p^+),\, \boldsymbol{x}_s \in W^s(p^-), \text{ and } \|\boldsymbol{x}_u - \boldsymbol{x}_s\|_\infty < \varepsilon \right\}.$$

Here, the choice of the accuracy parameter ε should be informed by the accuracy parameters of the computation of the manifolds. Note that we use the L_∞-norm (in compactified coordinates) for computational efficiency. In each ε-cube (which defines a ball in the L_∞-norm) around a point in Ψ_ε, we find segments of both $W^u(p^+)$ and $W^s(p^-)$. To determine the set Ψ_ε in practice, we consider pairs of points $(\boldsymbol{x}_u, \boldsymbol{x}_s) \in \mathbb{R}^3 \times \mathbb{R}^3$ in the respective mesh representations of $W^u(p^+)$ and $W^s(p^-)$ computed with the algorithm from [12]. We then employ the MATLAB function `ismembertol`, which sorts the meshes lexicographically before finding all points within a certain distance of each other with respect to the L_∞-norm. By definition, the points in Ψ_ε are then computed as the average of the mesh points in $W^u(p^+)$ and $W^s(p^-)$ that lie to within distance ε of each other.

Figure 6 depicts, in non-compactified coordinates, the set Ψ_ε with $\varepsilon = 10^{-3}$ in magenta, together with $\cup_{i=5}^{26}\mathsf{Per}^i$ in green, which represents the the maximal invariant set Λ. Notice that points in Ψ_ε closely align with the overall shape of $\cup_{i=5}^{26}\mathsf{Per}^i$, that is, $\mathrm{cl}\,(\mathsf{Per})$ and, thus, Λ seem to lie in the intersection of the closures of $W^u(p^+)$ and $W^s(p^-)$.

5.1 Finding non-transverse heterodimensional connecting orbits

The set Ψ_ε does not contain exact intersection points. However, we can use it to obtain a suitable approximation of a non-transverse heteroclinic orbit from p^+ to p^- that can be refined with Newton's method as the approximate solution to an appropriate boundary value problem (BVP). Our set-up is similar to the approach taken by Beyn and Kleinkauf [4]; see also [25]. We formally define the heteroclinic orbit, denoted $\mathcal{A}$, as an orbit segment of length $N_u + N_s + 1$, for sufficiently large integers $N_u, N_s \in \mathbb{N}$, given by

$$\mathcal{A} := \{a_{-N_u}, \ldots, a_{-1}, a_0, a_1, \ldots, a_{N_s}\},$$

where

$$T(a_i) = a_{i+1}, \quad \text{for } i = -N_s, \ldots, N_u - 1. \tag{6}$$

To ensure that $\mathcal{A}$ approximates a connecting orbit, the first point a_{-N_s} must lie close to p^+ on its one-dimensional unstable eigenspace. Similarly, the final point a_{N_s} must lie near p^- on its one-dimensional stable eigenspace of p^-. We express these two requirements in the form of the following boundary conditions

$$a_{-N_u} = p^+ + \delta_u\, \mathbf{v}_u, \tag{7}$$

and

$$a_{N_s} = p^- + \delta_s\, \mathbf{v}_s, \tag{8}$$

where $\mathbf{v}_u$ and $\mathbf{v}_s$ are the unit unstable and stable eigenvectors of p^+ and p^-, respectively, and the real parameters δ_u and δ_s measure the respective distances of a_{-N_s} to p^+ and a_{N_u} to p^-. For $\mathcal{A}$

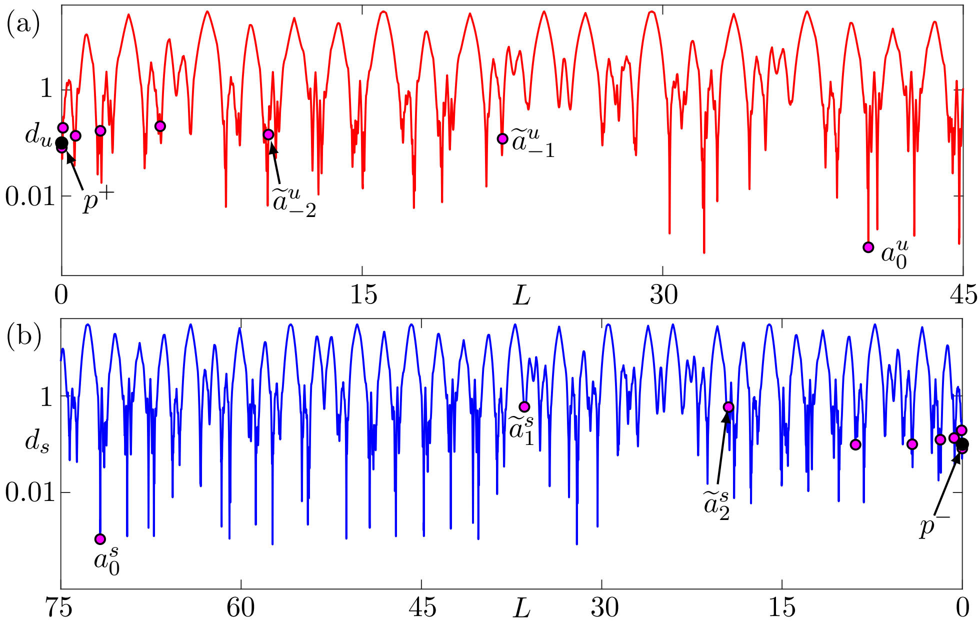

Figure 7: Minimal Euclidean distances between $W^u(p^+)$ and $W^s(p^-)$ in compactified coordinates. Panel (a) shows the minimal distance d_u (red curve) from a point in $W^u(p^+)$ to the first part of $W^s(p^-)$ up to arclength $L = 80$, parameterized by arclength along $W^u(p^+)$. Similary, panel (b) shows the minimal distance d_s (blue curve) from $W^s(p^-)$ to the first part of $W^u(p^+)$. Also shown are pseudo-orbits $\{\widetilde{a}^u_i\}_{-13\leq i\leq -1}$ and $\{\widetilde{a}^s_i\}_{1\leq i\leq 14}$ (magenta dots) to and from the local minima a^u_0 of d_u and a^s_0 of d_s, respectively.

to be a good approximation, δ_u and δ_s need to be sufficiently small. The overall BVP (6)–(8); comprises $3(N_u + N_s) + 6$ equations, namely, the $N_u + N_s$ three-dimensional mapping conditions from (6), and the two three-dimensional boundary conditions from (7) and (8). To solve this BVP, one needs to find the $3(N_u + N_s + 1)$ coordinates of the points in $\mathcal{A}$, as well as the distance parameters δ_u and δ_s, which gives a total of $3(N_u + N_s) + 5$ unknowns. Hence, to ensure this BVP is well posed and has a locally unique solution, we allow the single parameter k to be solved for as well; this reflects the fact that the heterodimensional connecting orbit we are seeking is of codimension one; see again also [4, 25].

We construct a seed solution from a point in Ψ_ε by considering the corresponding mesh points in $W^u(p^+)$ and $W^s(p^-)$, as well as their backward and forward trajectories, respectively. We obtain such trajectories as pseudo-orbits [29] along the computed meshes of $W^u(p^+)$ and $W^s(p^-)$ with the method from [11]. For each computed mesh point of $W^u(p^+)$ the algorithm stores a pointer to another mesh point that is an approximate preimage. Consequently, for any point in the mesh representing $W^u(p^+)$, we can follow the pointers backwards towards p^+, and the resulting sequence of points constitutes a pseudo-orbit for T. How close the pseudo-orbit is to an actual orbit depends on the accuracy parameters of the manifold computation; see [11] for specific details. Similarly, we obtain a pseudo-orbit to p^- for any mesh point in the computed part of $W^s(p^-)$.

Figure 7 illustrates our approach by showing the shortest distance $d_u(L)$ of the point at arclength L in $W^u(p^+)$ to any point in the first part of $W^s(p^-)$ up to arclength $L_{\max} = 80$; and likewise for $d_s(L)$. More specifically, for arclength parameterizations $w_u(L)$ for $W^u(p^+)$ and $w_s(L)$

for $W^s(p^-)$, we define

$$\begin{aligned} d_u(L) &= \min_{\ell < L_{\max}} \|w_u(L) - w_s(\ell)\| \quad \text{and} \\ d_s(L) &= \min_{\ell < L_{\max}} \|w_s(L) - w_u(\ell)\|. \end{aligned}$$

Here, we use the Euclidean norm, still in compactified coordinates. Figure 7 shows $d_u(L)$ for L increasing from 0 to 45 in panel (a), and similarly, $d_s(L)$ for L decreasing from 75 to 0 in panel (b). Observe that the curve in panel (a) respects the symmetry (3) with the curve for $0 \leq L \leq 45$ shown in panel (b); hence, $d_u(L) = d_s(L)$ if both are computed for the same $L_{\max}$. Each local minimum in d_u is associated with exactly one specific local minimum in d_s, and together they represent a pair of points in $W^u(p^+)$ and $W^s(p^-)$ that are close in phase space. For the selected pair a_0^u and a_0^s in Fig. 7, we have $\|a_0^s - a_0^u\| \approx 3 \times 10^{-2}$. Panels (a) and (b) also show the pseudo-orbits $\{\widetilde{a}_{-13}^u, \ldots, \widetilde{a}_{-1}^u, a_0^u\}$ and $\{a_0^s, \widetilde{a}_1^s, \ldots, \widetilde{a}_{14}^s\}$ generated from a_0^u and a_0^s, respectively; note that these points are near, but not exactly on, the local minima of d_u and d_s. We remark that the pair (a_u^0, a_s^0) was chosen for illustrative purposes; the same construction works for any pair of nearby points in $W^u(p^+)$ and $W^s(p^-)$, which typically leads to a different connecting orbit for a (slightly) different k-value.

The two pseudo-orbits are concatenated at $a_0^u \approx a_0^s$ to give the approximate non-transverse heteroclinic orbit

$$\widetilde{\mathcal{A}} := \{\widetilde{a}_{-N_u}, \ldots, \widetilde{a}_0, \ldots, \widetilde{a}_{N_s}\} = \{\widetilde{a}_{-13}^u, \ldots, \widetilde{a}_{-1}^u, a_0^u, \widetilde{a}_1^s, \ldots, \widetilde{a}_{14}^s\},$$

with $N_u = 13$ and $N_s = 14$. We remark that the choice $\widetilde{a}_0 = a_0^u$ is for definiteness; one could instead choose a_0^s or the average of these two points.

With $\widetilde{\mathcal{A}}$ as a seed, Newton's method converges to a solution

$$\mathcal{A} = \{a_{-13}, \ldots, a_{-1}, a_0, a_1, \ldots, a_{14}\}$$

of the BVP (6)–(8), and we find that $k = \sqrt{20}$ has now been adjusted slightly to $k = k^* \approx \sqrt{20} + 5.027 \times 10^{-4}$.

Figure 8 shows the computed non-transverse heterodimensional orbit $\mathcal{A}$ for $k = k^*$. Panel (a) shows $W^u(p^+)$ and $W^s(p^-)$ in $\mathbb{B}^3$, up to their first intersection point a_0. In addition, we show the points in $\mathcal{A}$, with only a_{-1}, a_0, and a_1 labeled, together with local intersecting segments of $W^u(p^+)$ and $W^s(p^-)$. Panel (b) shows the computed heterodimensional connecting orbit $\mathcal{A}$ in non-compactified coordinates, again with the corresponding intersecting local manifold segments. Notice that the start and end points of $\mathcal{A}$ are very close to p^+ and p^-, respectively, which illustrates the accuracy of this connection.

5.2 Finding transverse return connecting orbits

To complete the heterodimensional cycle for T at $k = k^*$, we also compute the intersection of the two-dimensional manifolds $W^u(p^-)$ and $W^s(p^+)$ for the same parameter value. Generically, $W^u(p^-) \cap W^s(p^+)$ has dimension one and consists of infinitely many return orbits from p^- to p^+. As before, we choose suitable integers $N_u, N_s \in \mathbb{N}$ and represent one particular return orbit $\mathcal{B} \in W^u(p^-) \cap W^s(p^+)$ as the orbit segment

$$\mathcal{B} := \{b_{-N_u}, \ldots, b_{-1}, b_0, b_1, \ldots, b_{N_s}\},$$

where

$$T(b_i) = b_{i+1}, \quad \text{for } i = -N_s, \ldots, N_u - 1. \tag{9}$$

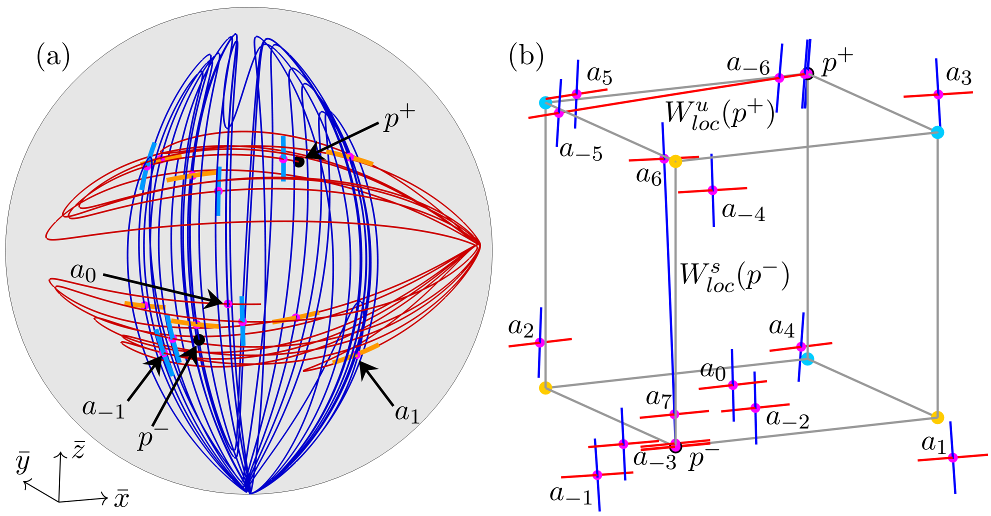

Figure 8: The heteroclinic orbit $\mathcal{A} = \{a_i\}_{-13\leq i\leq 14}$ (purple points) from p^+ to p^- for $k^* \approx \sqrt{20} + 5.027 \times 10^{-4}$. Panel (a) shows in $\mathbb{B}^3$ the one-dimensional manifolds $W^u(p^+)$ (red) and $W^s(p^-)$ (blue) until their first point of intersection a_0; local intersecting segments (orange and light blue) are shown at all other points a_i. Panel (b) shows $\mathcal{A}$ in $\mathbb{R}^3$ with the respective local segments of intersecting manifolds.

In this case, the boundary conditions take the form

$$b_{-N_u} = p^- + \delta_u\,\mathbf{v}_u + \delta_{uu}\,\mathbf{v}_{uu}, \tag{10}$$

and

$$b_{N_s} = p^+ + \delta_s\,\mathbf{v}_s + \delta_{ss}\,\mathbf{v}_{ss}. \tag{11}$$

Here, $\mathbf{v}_u$ and $\mathbf{v}_{uu}$ are unit vectors that span the two-dimensional unstable eigenspace of p^-, and similarly, $\mathbf{v}_s$ and $\mathbf{v}_{ss}$ span the stable eigenspace of p^-. Note that there are now two pairs of distance parameters δ_u, δ_{uu}, and δ_s, δ_{ss} which control the distances along the respective eigendirections. In total, the BVP (9)–(11) has $3(N_u + N_s) + 6$ equalities for $3(N_u + N_s) + 7$ unknowns. Hence, this BVP is under-determined and its solution family comprises a one-dimensional intersection set; unlike for the non-transverse case, we keep the parameter $k = k^*$ fixed.

To solve the BVP (9)–(11), we again require an approximate orbit as a seed solution. Finding such a seed in $W^u(p^-) \cap W^s(p^+)$ is challenging because computing manifolds of dimension two is far more difficult than for the one-dimensional case [30]. However, for our purposes, we are not interested in the precise geometry of the global manifolds; instead, we only want to find where the manifolds come close to each other so that we can find a point approximately in their intersection set. Such seed points only need to be sufficiently accurate so that the BVP converges with Newton's method.

Figure 5.2 shows how we identify candidate points in $W^u(p^-) \cap W^s(p^+)$. First, we find a localized approximation of each of the two-dimensional manifolds by applying T or T^{-1} to a mesh representation of a local patch in the eigenspaces of p^- and p^+. More precisely, in $E^u(p^-)$ we start with a 200×200 uniform mesh in the parallelogram spanned by $\mathbf{v}_u$ and $\mathbf{v}_{uu}$ with side lengths $l_u = l_{uu} = 0.5$. We then map this mesh twice by T and obtain surfaces by triangulation of the resulting mesh points. Fig. 5.2(a) shows this surface along with image patches representing $W^s(p^+)$, generated similarly from a patch on $E^s(p^+)$. Observe that the surfaces approximating $W^u(p^-)$ and $W^s(p^+)$ intersect near two of the bottom corners of the cube. We identify b_0^u and b_0^s

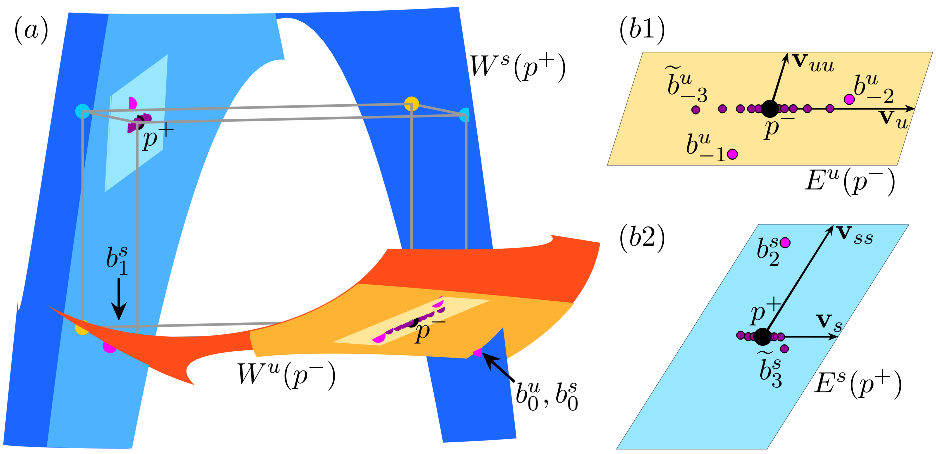

Figure 9: Approxmiate patches of the two-dimensional manifolds $W^u(p^-)$ and $W^s(p^+)$ in $\mathbb{R}^3$ for $k = k^* \approx \sqrt{20} + 5.027 \times 10^{-4}$. Panel (a) shows the cube of $p^\pm$ and $q^\pm$, with patches of local eigenspaces $E^u(p^-)$ (cyan parallelogram) and $E^s(p^+)$ (pale orange parallelogram), together with their first and second images under T (orange and red surfaces) and T^{-1} (light- and dark-blue surfaces), respectively. Also shown are the orbit segments $\{b_i^u\}_{-2\le i\le 0}$ and $\{b_i^s\}_{0\le i\le 2}$ (magenta points), and the pseudo-orbits of their tails $\{\widetilde{b}_i^u\}_{-26\le i\le -3}$ and $\{\widetilde{b}_i^s\}_{3\le i\le 24}$ (dark purple points). Panels (b1) and (b2) show the points on the local patches in $E^u(p^-)$ and $E^s(p^+)$, respectively.

as the pair of closest mesh points on $W^u(p^-)$ and $W^s(p^+)$, and construct the orbit segments

$$\begin{aligned} \{b^u_{-2}, b^u_{-1}, b^u_0\} &= \{T^{-2}(b^u_0),\, T^{-1}(b^u_0),\, b^u_0\} \quad \text{and} \\ \{b^s_0, b^s_1, b^s_2\} &= \{b^s_0,\, T(b^s_0),\, T^2(b^s_0)\}\,. \end{aligned}$$

By definition, the second (pre-)images b^u_{-2} and b^s_2 lie in $E^u(p^-)$ and $E^s(p^+)$, respectively. Hence, we can apply the linearized map to extend the orbit segments to the pseudo-orbit

$$\widetilde{\mathcal{B}} := \left\{\widetilde{b}^u_{-26}, \dots, \widetilde{b}^u_{-3}, b^u_{-2}, b^u_{-1}, b^u_0, b^s_1, b^s_2, \widetilde{b}^s_3, \dots, \widetilde{b}^s_{24}\right\}.$$

Here, the points $\{\widetilde{b}^u_{-26}, \dots, \widetilde{b}^u_{-3}\}$ are added by using the Jacobian matrix $DT^{-1}(p^-)$ with subsequent projection onto the patch in $E^u(p^-)$; and the points $\{\widetilde{b}^s_3, \dots, \widetilde{b}^s_{24}\}$ are added similarly, by applying $DT(p^+)$. Panel (b1) in Fig. 5.2 shows $\{\widetilde{b}^u_{-26}, \dots, \widetilde{b}^u_{-3}, b^u_{-2}, b^u_{-1}\}$ on the patch in $E^u(p^-)$. Since the unstable eigenvalues of p^- are real and negative, the points $\{\widetilde{b}^u_{-26}, \dots, \widetilde{b}^u_{-3}, b^u_{-2}, b^u_{-1}\}$ tend to p^- from both sides of $\mathbf{v}_u$ and $\mathbf{v}_{uu}$. Panel (b2) shows the points $\{b^s_2, \widetilde{b}^s_3, \dots, \widetilde{b}^s_{24}\}$ on the patch in $E^s(p^+)$, which converge in a similar manner. By adding points in this way, we ensure $\widetilde{\mathcal{B}}$ begins and ends at points that lie within distance 10^{-3} from p^- and p^+, respectively, so that this pseudo-orbit may serve as a good approximation for a heteroclinic orbit connecting the two fixed points.

Since the BVP (9)–(11) is under-determined, we require an additional condition to get a unique solution. As a practical choice, we fix the distance

$$\eta = \|b_0 - p^-\|, \tag{12}$$

from p^- to b_0, and introduce η as a new parameter. When we solve the augmented BVP with Newton's method and keep η fixed, we find the single heteroclinic orbit

$$\mathcal{B} = \{b_{-26}, \dots, b_0, \dots, b_{24}\} \subset W^u(p^-) \cap W^s(p^+).$$

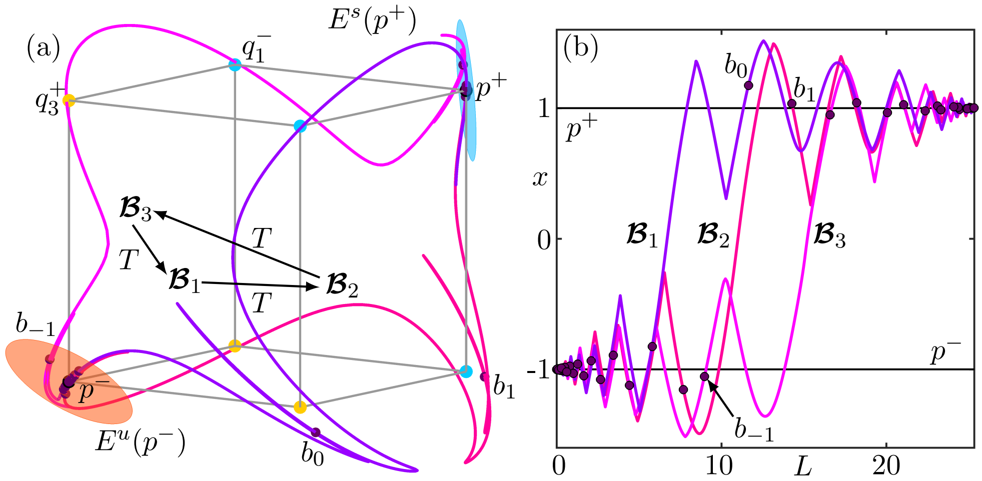

Figure 10: The family of heteroclinic orbits $\boldsymbol{\mathcal{B}} = \boldsymbol{\mathcal{B}}_1 \cup \boldsymbol{\mathcal{B}}_2 \cup \boldsymbol{\mathcal{B}}_3 \subseteq W^u(p^-) \cap W^s(p^+)$ from p^- to p^+ for $k = k^* \approx \sqrt{20} + 5.027 \times 10^{-4}$. Panel (a) shows the curves $\boldsymbol{\mathcal{B}}_1$ (magenta), $\boldsymbol{\mathcal{B}}_2$ (dark purple), and $\boldsymbol{\mathcal{B}}_3$ (light purple), along with the particular heteroclinic orbit $\mathcal{B} = \{b_i\}_{-26 \leq i \leq 24}$ (dark purple points). Also shown as small disks are the two-dimensional local eigenspaces $E^u(p^-)$ (orange) and $E^s(p^+)$ (light blue). Panel (b) shows the x-coordinates of all points in each of the curves $\boldsymbol{\mathcal{B}}_i$, for $i = 1, 2, 3$, versus arclength L.

To compute the entire heteroclinic intersection set, we continue $\mathcal{B}$ in the parameter η of (12). We ensure that the solution at each continuation step remains accurate by monitoring the distances $\delta_u^2 + \delta_{uu}^2$ and $\delta_s^2 + \delta_{ss}^2$ of the two end points in the orbit segment to their respective fixed point.

Figure 10 depicts the result of this continuation starting from B. More precisely, we find that the entire η-parameterized family of orbits forms three smooth, continuous curves, denoted $\boldsymbol{\mathcal{B}} := \boldsymbol{\mathcal{B}}_1 \cup \boldsymbol{\mathcal{B}}_2 \cup \boldsymbol{\mathcal{B}}_3 \subseteq W^u(p^-) \cap W^s(p^+)$; these are shown in panel (a) together with the two-dimensional local eigenspaces (orange and light-blue disks) at P^- and p^+, respectively. Panel (b) shows each curve $\boldsymbol{\mathcal{B}}_i$, for $i = 1, 2, 3$, in terms of their x-coordinates versus arclength L. All three curves emanate from p^- tangent to its two-dimensional local unstable eigenspace $E^u(p^-)$, and end by converging to p^+ along its two-dimensional stable eigenspace $E^s(p^+)$. Moreover, owing to the negative real eigenvalues, the curves spiral around the respective fixed points. The oscillating nature of $\boldsymbol{\mathcal{B}}_1$, $\boldsymbol{\mathcal{B}}_2$ and $\boldsymbol{\mathcal{B}}_3$ near p^- and p^+ is not very visible in panel (a), but is highlighted with respect to their x-coordinates in the alternative arclength representation in panel (b). The curves $\boldsymbol{\mathcal{B}}_1$, $\boldsymbol{\mathcal{B}}_2$ and $\boldsymbol{\mathcal{B}}_3$ map to each other, that is, they can be ordered such that

$$\boldsymbol{\mathcal{B}}_1 \xmapsto{T} \boldsymbol{\mathcal{B}}_2 \xmapsto{T} \boldsymbol{\mathcal{B}}_3 \xmapsto{T} \boldsymbol{\mathcal{B}}_1.$$

Moreover, the reversibility R (3) also acts on these curves, namely,

$$\boldsymbol{\mathcal{B}}_1 \xmapsto{R} \boldsymbol{\mathcal{B}}_2 \xmapsto{R} \boldsymbol{\mathcal{B}}_1 \quad \text{and} \quad \boldsymbol{\mathcal{B}}_3 \xmapsto{T} \boldsymbol{\mathcal{B}}_3.$$

This symmetry is reflected in Fig. 10 by $\boldsymbol{\mathcal{B}}_1$ and $\boldsymbol{\mathcal{B}}_2$ having the same shape, including a particularly sharp excursion near b_0 and b_1, respectively. Note that, the curve $\boldsymbol{\mathcal{B}}_3$ comes very close to q_3^+ and q_1^-, but does not include these points.

Figure 11 shows the overall heterodimensional cycle $\mathcal{A} \cup \boldsymbol{\mathcal{B}}$ for $k = k^* \approx \sqrt{20} + 5.027 \times 10^{-4}$. In the same figure, we also show the set $\cup_{i=5}^{26} \mathsf{Per}_i$ computed for $k = k^*$. The set of periodic points with periods less than 26 for $k = k^*$ is effectively the same as the one from Fig. 2 for $k = \sqrt{20}$, and it is again a good representation of the maximal invariant set Λ for this value of $k = k^*$. By definition, both the codimension-one orbit $\mathcal{A}$ and the family $\boldsymbol{\mathcal{B}}$ of return connections lie in

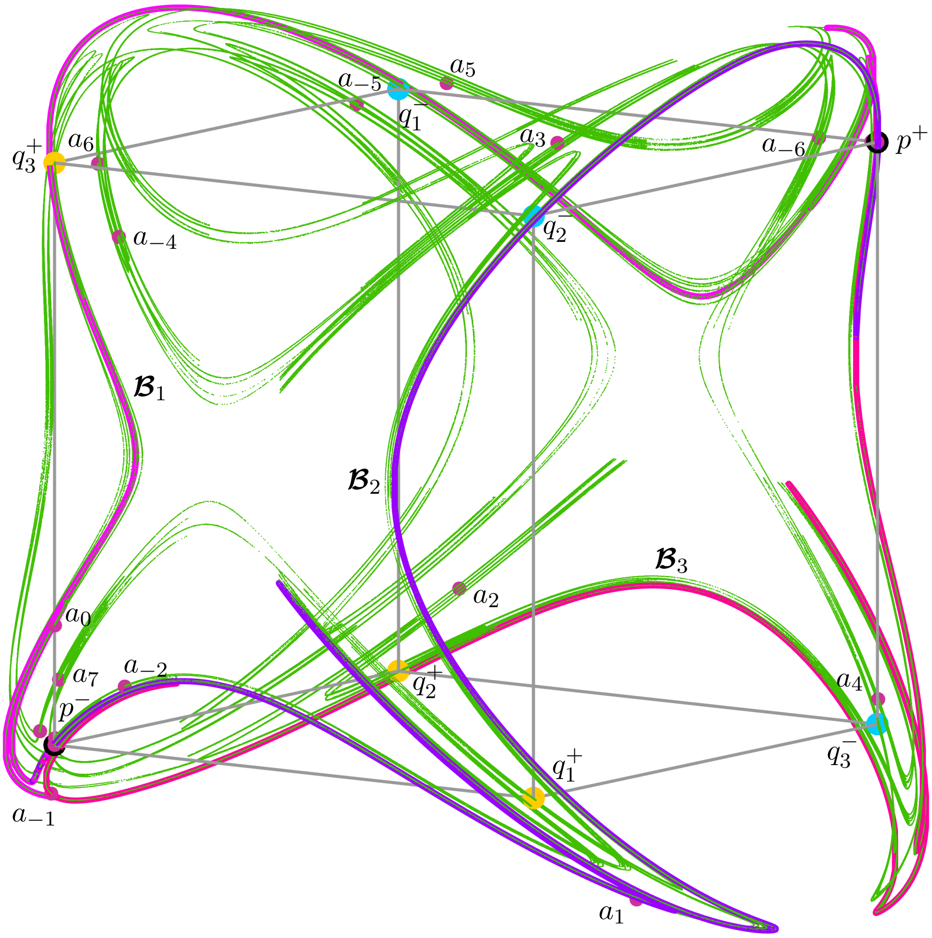

Figure 11: The heterodimensional cycle of T for $k = k^* \approx \sqrt{20} + 5.027 \times 10^{-4}$ consisting of the non-transverse connecting orbit $\mathcal{A} = \{a_i\}_{-13 \leq i \leq 14}$ and the family $\boldsymbol{\mathcal{B}}$ of transverse return orbits comprising the curves $\boldsymbol{\mathcal{B}}_1$ (magenta), $\boldsymbol{\mathcal{B}}_2$ (dark purple), and $\boldsymbol{\mathcal{B}}_3$ (light purple). Also shown is Λ as represented by $\cup_{i=5}^{26}\mathsf{Per}_i$. See also the accompanying animation (dko_hetdim_anim_fig11.mp4 [2MB]).

$\Lambda = \mathrm{cl}(\mathsf{Per})$. Notice further that $\boldsymbol{\mathcal{B}}$ 'traces out' three of the curves along which the periodic points align. We remark that the λ-lemma [29] requires the two-dimensional manifolds $W^u(p^-)$ and $W^s(p^+)$ to follow the heterodimensional cycle $\mathcal{A} \cup \boldsymbol{\mathcal{B}}$ around, producing further intersections [42]; these additional intersections must also be part of Λ. Indeed, we conjecture that Λ is also given by the closure of the entire (much larger) intersection set $W^u(p^-) \cap W^s(p^+)$ of the two two-dimensional manifolds.

6 Conclusions

We presented an extensive case study of the shear-rotation map (1) for the fixed parameter value $k = \sqrt{20}$ to characterize its maximal invariant set. Specifically, we computed millions of period-n points, namely, all periodic orbits with for $n \leq 26$, and separated them by index for $n \leq 23$. We also computed the one-dimensional manifolds $W^u(p^+)$ and $W^s(p^-)$ of the two fixed points up to very long arclengths and, by allowing k to vary slightly, located with a boundary-value problem setup both a codimension-one heteroclinic orbit and a one-dimensional family of return connections between p^+ and p^-. We can summarize our findings as the following mathematical observations for the map T at $k = \sqrt{20}$:

- **I** *Intermingled maximal Invariant Set:* The (globally) maximal invariant set Λ of T lies inside the box $B = [-2, 2]^3$. It is the closure of both Per_1 and Per_2, which are the sets of index-one and -two periodic orbits, respectively. Hence, Λ is not hyperbolic and and the set is intermingled with respect to its index.

- **C** *Carpet property:* The one-dimensional manifolds $W^u(p^+)$ and $W^s(p^-)$ of the fixed points $p^\pm$ are both dense in suitable projections. Consequently, they have the carpet property, implying that their closures intersect robustly.

- **R** *Robust heterodimensional cycles:* $W^u(p^+)$ and $W^s(p^-)$ intersect at $k = k^*$ very close to $k = \sqrt{20}$, forming a non-transverse heteroclinic orbit from p^+ to p^-. Moreover, the two-dimensional manifolds $W^u(p^-)$ and $W^s(p^+)$ intersect transversely at $k = k^*$, so T has a heterodimensional cycle between p^+ and p^-. Since $W^u(p^+)$ and $W^s(p^-)$ have the carpet property, there exists a dense set of k-values in an interval around $k = \sqrt{20}$, for which $W^u(p^+) \cap W^s(p^-) \neq \emptyset$. By taking the closure, it follows that T has robust heterodimensional cycles near $k = \sqrt{20}$.

These observations are based on results obtained with accurate numerical methods that have established error bounds. While they have the status of conjectures, the underlying computations can, in principle, be made rigorous with interval arithmetic tools to obtain computer-assisted proofs [10, 28].

The parameter value $k = \sqrt{20}$ is not special. Indeed, our investigation showed that the dynamics are structurally the same for other values of k near $\sqrt{20}$. However, for $k = 0$ the map T reduces to a simple rotation, and a natural question is: how do the complicated nonhyperbolic structures, including Λ and heterodimensional cycles, disappear as k is decreased? We are actively pursuing this research direction, and the results will be reported in a separate publication.

We studied the map T from the global perspective by revealing the properties of its entire maximal invariant set Λ. Since Λ is not hyperbolic, it cannot be a blender. On the other hand, the robust existence of heterodimensional cycles in Λ suggests that some local part of Λ should be a blender, that is, a transitive hyperbolic set with the carpet property. This blender should be a locally maximal invariant set that only contains periodic orbits of a single index. Taking a simple neighbourhood around a fixed point or period-three orbit of the map T does not yield such a hyperbolic set. However, initial explorations reveal that it may be possible to identify a blender by considering a more elaborate open set. Taking this more local perspective is ongoing work that will be reported elsewhere.

The map T is only one example of a dynamical system in $\mathbb{R}^3$ with robust heterodimensional cycles. Nevertheless, we believe that its properties are generic in the sense that the properties **I**, **C**, and **R** above will also be found for other three-dimensional diffeomorphisms with robust heterodimensional cycles. Indeed, the numerical approach presented here can be used in the same spirit to check this assertion for any other explicitly given diffeomorphism.

Acknowledgments

We thank Andy Hammerlindl, Katsutoshi Shinohara, and Warwick Tucker for many helpful discussions. We particularly thank Andy and Warwick for their hospitality when hosting all of us at Monash University at various occasions. We are grateful to Dana C'Julio for advice on the manifold computations. This work was funded by the Royal Society Te Apārangi Marsden Fund grant #22-UOA-204.

A Finding periodic orbits of high periods and their spectrum

In [32], period-n points were found with Newton's method as solutions of

$$T^n(\boldsymbol{x}) - \boldsymbol{x} = \boldsymbol{0}. \tag{13}$$

Due to the saddle nature of the periodic points, Newton's method will only converge if seeds are chosen very close to a periodic point, especially as n increases. The method employed in [32] involved an exhaustive search over the subset $[-2, 2]^3$ of phase space; in particular, the Honours student found 1,329 period-11 points, which reportedly took three days. Hence, this approach is not suitable for finding Per^n for large n.

To overcome this issue, we solve for all points in a period-n orbit simultaneously. More precisely, a period-n orbit of T, given by

$$\boldsymbol{x}_1 = \begin{pmatrix} x_1 \\ y_1 \\ z_1 \end{pmatrix} \mapsto \boldsymbol{x}_2 = \begin{pmatrix} x_2 \\ y_2 \\ z_2 \end{pmatrix} \mapsto \ldots \mapsto \boldsymbol{x}_n = \begin{pmatrix} x_n \\ y_n \\ z_n \end{pmatrix} \mapsto \boldsymbol{x}_1 = \begin{pmatrix} x_1 \\ y_1 \\ z_1 \end{pmatrix}.$$

is a solution of the $3n$-dimensional system

$$\begin{pmatrix} \boldsymbol{x}_2 \\ \vdots \\ \boldsymbol{x}_i \\ \vdots \\ \boldsymbol{x}_1 \end{pmatrix} = \begin{pmatrix} T(\boldsymbol{x}_1) \\ \vdots \\ T(\boldsymbol{x}_{i-1}) \\ \vdots \\ T(\boldsymbol{x}_n) \end{pmatrix}.$$

By making use of the special form of T, we can simplify this to the n-dimensional system

$$\begin{pmatrix} x_1 \\ x_2 \\ x_3 \\ \vdots \\ x_i \\ \vdots \\ x_n \end{pmatrix} = \begin{pmatrix} x_{n-2} + k({x_n}^2 + {x_{n-1}}^2 - 2) \\ x_{n-1} + k({x_1}^2 + {x_n}^2 - 2) \\ x_n + k({x_2}^2 + {x_1}^2 - 2) \\ \vdots \\ x_{i-3} + k({x_{i-1}}^2 + {x_{i-2}}^2 - 2) \\ \vdots \\ x_{n-3} + k({x_{n-1}}^2 + {x_{n-2}}^2 - 2) \end{pmatrix}, \tag{14}$$

with the y- and z-coordinates of points in the period-n orbit given by

$$\begin{aligned} (y_1, y_2, \ldots, y_n) &= (x_n, x_1, \ldots, x_{n-1}), \\ (z_1, z_2, \ldots, z_n) &= (x_{n-1}, x_n, \ldots, x_{n-2}). \end{aligned}$$

System (14) has two symmetries: cyclically permuting $(x_1, \ldots, x_n)$ does not change the equations because the point $\boldsymbol{x}_1$ can be any point in the period-n orbit; furthermore, if $(x_1, \ldots, x_n)$ is a solution of (14) then so is $(-x_n, -x_{n-1}, \ldots, -x_1)$, which is a consequence of the reversibility R (3).

When solving (14), Newton's method converges with seeds that may lie quite far from true periodic orbits. According to [20, Theorem 3.1], the quadratic system (14) has 2^n possible solutions. Consequently, T has at most 2^n period-n points, which motivates us to generate the 2^n elements of $\{-1, 1\}^n$ as seeds for finding all period-n orbits, up to cyclic permutation. This filtering of $\{-1, 1\}^n$ is achieved by the *Necklace algorithm* from [19]. With these seeds, we solve the n-dimensional system (14) numerically with the Julia package `NLSolve` to find all period-n

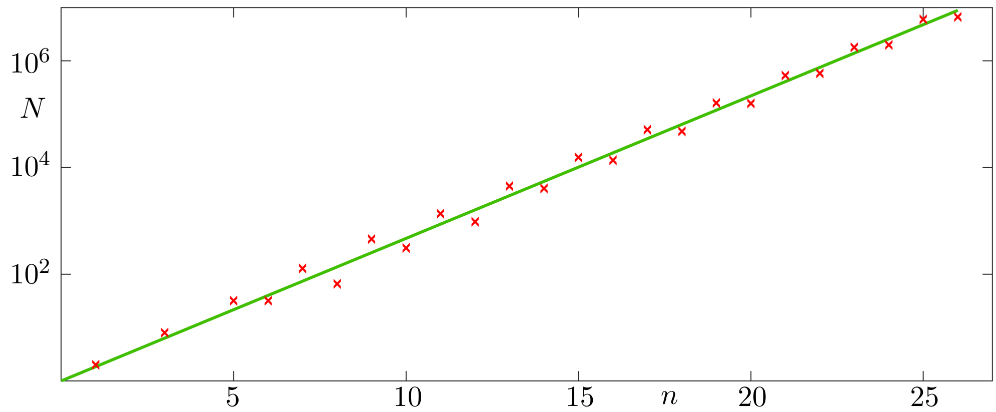

Figure 12: The number $N = |\overline{\mathsf{Per}^n}| = \Sigma_{d|n}^n |\mathsf{Per}^d|$ (red crosses) of all period-n points against their period n, shown together with the best linear fit (green).

orbits. Note that the resulting solution set includes period-d orbits for periods d that are divisors of n; we remove such periodic orbits in a post-processing step to obtain the set Per^n of periodic orbits with minimal period n. The second and fourth columns of Table 1 respectively list the total number of period-n points and the time it took to find them. For $n \leq 10$, our results agree with [32], and we find 33 additional points in Per^{11}. Importantly, the computation time is greatly reduced: with our implementation, we find all 1,364 period-11 points in under 0.01 seconds on a desktop computer, and all points in $\cup_{i=5}^{26}\mathsf{Per}^i$ are found in fewer than 15 minutes.

We observe that all periodic points in $\cup_{i=5}^{26}\mathsf{Per}^i$ are found. To confirm this, we make use of the polynomial nature of (14) and employ homotopy continuation using the Julia package `HomotopyContinuation.jl` [8]. More specifically, we begin with the n-dimensional system of polynomials $F(x_1, \ldots, x_n) = \left(x_1^2 - 1, \ldots, x_n^2 - 1\right)$, for wich our seeds are the actual and entire solution family, and continue the solutions to those of (14). Crucially, note that F and (14) have the same degree. In this way, we verify that our method finds all period-n points for $n \leq 19$. For $n = 19$, this computation already takes 20 minutes, and given the exponentially increasing computation time with increasing period, it is impractical to use homotopy continuation for higher periods. Nevertheless, it gives us confidence that our method finds all period-n points for $n \leq 26$.

Further support of this statement is presented in Fig. 12. Here, we show on a logarithmic scale versus n, the number N of all period-n points, including those with smaller least periods. We find that this relationship is linear, as is shown by the line representing the least-squares fit of the data. The data points come in consecutive pairs; the number of odd and even periods lie slightly above and below the line of best fit, respectively. Indeed, the lack of outliers in this systematic picture provides further evidence that we can find all points in Per^n.

The growth rate of the number of periodic points

Figure 12 allows us to estimate the exponential growth rate of the periodic points by considering the sequence

$$g_T^{(n)} = \frac{\log N}{n},$$

which is shown for $5 \leq n \leq 26$ in Table 1. In fact, Fig. 12 suggests that there are two subsequences of $g_T^{(n)}$, namely, one for even and one for odd n. We estimate that $g_T^{(n)}$ approaches 0.604 and 0.624 for even and odd n, respectively. The overall limit

$$h_T = \lim_{n\to\infty} g_T^{(n)} \approx 0.615, \tag{15}$$

is given by the gradient of the linear least squares fit. Note that this value is very close to the average of the two subsequences, which each have limits that appear to converge to h_T very slowly.

The exponential growth of periodic points is closely related to topological entropy of the system [2]. Indeed, the entropy of a diffeomorphism with a hyperbolic maximal invariant set that is densely filled with periodic points is precisely given by (15). However, the maximal invariant set Λ is not uniformly hyperbolic, so it is not clear whether this formula applies for T. Nevertheless, our results give a very strong indication that the entropy of T is positive and, hence, the system exhibits chaotic dynamics [2].

Computing the spectrum of high-period orbits

To determine the index of a period-n orbit $\{\boldsymbol{x}_i\}_{1\leq i\leq n}$ we need to assess how many eigenvalues of the Jacobian matrix $DT^n(\boldsymbol{x}_1)$ have modulus larger than one. For large n, this computation is numerically sensitive: strong unstable eigenvalues become very large and strong stable eigenvalues become very small, while weak eigenvalues are near 1 in modulus. The loss of precision for the central eigenvalues makes it hard to determine how many have modulus larger than one. To address this problem, we use 32 digits of precision in MATLAB to compute the spectrum of a period-n orbit by calculating $DT^n(\boldsymbol{x}_1)$ as the product of the Jacobians $DT(\boldsymbol{x}_1)\,DT(\boldsymbol{x}_2)\,\cdots\,DT(\boldsymbol{x}_n)$. We employ the MATLAB function `eig` to determine the eigenvalues of this increased-precision Jacobian.

We find equal numbers of index-one and index-two period-n points for all periods $n \leq 23$, as expected from the symmetry (3); see panels (b1) and (b2) of Fig. 2. This serves as an independent test that 32 digits of precision are sufficient to separate the points with periods up to 23 by their index. This precision is no longer sufficient to determine the index for periods beyond 23, which itself takes almost three hours; details of how the computation time scales with the period n of the orbit are shown in the last column of Table 1.

References

[1] R. Abraham and S. Smale, "Nongenericity of Ω-stability," in S. Smale and S. S. Chern (eds.), *Global Analysis*, Proceedings of Symposia in Pure Mathematics Vol. 14, American Mathematical Society, Providence, RI, 1970, pp. 5–8.

[2] R. L. Adler, A. G. Konheim, and M. H. McAndrew, "Topological entropy," *Transactions of the American Mathematical Society* **114**(2): 309–319, 1965.

[3] D. V. Anosov, "Geodesic flows on closed closed Riemannian manifolds of negative curvature," *Trudy Matematicheskogo Instituta imeni V. A. Steklova* **90**: 3–210, 1967; English translation in *Proceedings of the Steklov Institute of Mathematics* Vol. 90, American Mathematical Society, Providence, RI, 1969, pp. 1–235.

[4] W.-J. Beyn and J.-M. Kleinkauf, "The numerical computation of homoclinic orbits for maps," *SIAM Journal on Numerical Analysis* **34**(3): 1207–1236, 1997.

[5] C. Bonatti, S. Crovisier, L. J. Díaz, and A. Wilkinson, "What is... a blender?" *Notices of the American Mathematical Society* **63**(10): 1175–1178, 2016.

[6] C. Bonatti and L. J. Díaz, "Persistent nonhyperbolic transitive diffeomorphisms," *Annals of Mathematics* **143**(2): 357–396, 1996.

[7] C. Bonatti, L. J. Díaz, and M. Viana, *Dynamics Beyond Uniform Hyperbolicity*, Encyclopaedia of Mathematical Sciences, Springer Berlin, Heidelberg, 2004.

[8] P. Breiding and S. Timme, "`HomotopyContinuation.jl`: A package for homotopy continuation in Julia," available via `https://www.juliahomotopycontinuation.org`, 2018.

[9] M. Brin and G. Stuck, *Introduction to Dynamical Systems*, Cambridge University Press, 2004.

[10] M. J. Capiński, B. Krauskopf, H. M. Osinga, and P. Zgliczyński, “Characterising blenders via covering relations and cone conditions,” *Journal of Differential Equations* **416**(1): 768–805, 2025.

[11] D. C’Julio, S. Amani, S. Doak, B. Krauskopf, and H. M. Osinga, “Constructing pseudo-orbits on invariant manifolds of maps as seeds for boundary value problems,” in J. Cushing, S. Elaydi, W. Zhang and B. Zheng (eds.) *Discrete Dynamical Systems, Difference Equations, and Applications, ICDEA 2025*, Springer Proceedings in Mathematics and Statistics, Springer, Cham, in press.

[12] D. C’Julio, B. Krauskopf, and H. M. Osinga, “Computing parametrised large intersection sets of 1D invariant manifolds: a tool for blender detection,” *Numerical Algorithms* **96**(3): 1079–1108, 2024 (ANODE 2023: In honour of John Butcher’s 90th birthday).

[13] C. Conley, “The gradient structure of a flow. I,” *Ergodic Theory and Dynamical Systems* **8**(8): 11–26, 1988; reprinting of IBM Research, RC 3932 (# 17806), Yorktown Heights, New York, 1972.

[14] M. Dellnitz, G. Froyland, and O. Junge, “The algorithms behind GAIO — Set oriented numerical methods for dynamical systems,” in B. Fiedler (ed.) *Ergodic Theory, Analysis, and Efficient Simulation of Dynamical Systems*, Springer, Berlin Heidelberg, 2001, pp. 145–174.

[15] R. L. Devaney, *An Introduction to Chaotic Dynamical Systems*, Taylor and Francis, 3rd ed., Philadelphia, PA, 2021.

[16] L. J. Díaz, “Robust nonhyperbolic dynamics and heterodimensional cycles,” *Ergodic Theory and Dynamical Systems* **15**(2): 291–315, 1995.

[17] L. J. Díaz, S. Kiriki, and K. Shinohara, “Blenders in centre unstable Hénon-like families: With an application to heterodimensional bifurcations,” *Nonlinearity* **27**(3): 353–378, 2014.

[18] L. J. Díaz and J. Rocha, “Nonconnected heterodimensional cycles: bifurcation and stability, *Nonlinearity* **5**(6): 1315–1342, 1992.

[19] H. Fredricksen and I. J. Kessler, “An algorithm for generating necklaces of beads in two colors,” *Discrete Mathematics* **61**(2): 181–188, 1986.

[20] C. B. Garcia and T. Y. Li, “On the number of solutions to polynomial systems of equations,” *SIAM Journal on Numerical Analysis* **17**(4): 540–546, 1980.

[21] J. Guckenheimer and P. Holmes, *Nonlinear Oscillations, Dynamical Systems, and Bifurcations of Vector Fields*, Applied Mathematical Sciences, Springer New York, NY, 1983.

[22] A. Hammerlindl, personal communication, 2026.

[23] A. Hammerlindl, B. Krauskopf, G. Mason, and H. M. Osinga, “Determining the global manifold structure of a continuous-time heterodimensional cycle,” *Journal of Computational Dynamics* **9**(3): 393–419, 2022.

[24] A. E. Hampton and J. D. Meiss, “Connecting anti-integrability to attractors for three-dimensional quadratic diffeomorphisms, *SIAM Journal on Applied Dynamical Systems* **23**(1): 616-640, 2024.

[25] S. Hittmeyer, B. Krauskopf, and H. M. Osinga, “Interacting global invariant sets in a planar map model of wild chaos,” *SIAM Journal on Applied Dynamical Systems* **12**(3): 1280–1329, 2013.

[26] S. Hittmeyer, B. Krauskopf, H. M. Osinga, and K. Shinohara, “Existence of blenders in a Hénon-like family: geometric insights from invariant manifold computations,” *Nonlinearity* **31**(10): R239–R267, 2018.

[27] S. Hittmeyer, B. Krauskopf, H. M. Osinga, and K. Shinohara, “How to identify a hyperbolic set as a blender,” *Discrete and Continuous Dynamical Systems* **40**(12): 6815–6836, 2020.

[28] T. Kapela, M. Mrozek, D. Wilczak, and P. Zgliczyński, “CAPD::DynSys: a flexible C++ toolbox for rigorous numerical analysis of dynamical systems,” *Communications in Nonlinear Science and Numerical Simulation* **101**: 105578, 2021.

[29] A. Katok and B. Hasselblatt, *Introduction to the Modern Theory of Dynamical Systems*, Encyclopedia of Mathematics and its Applications, Cambridge University Press, 1995.

[30] B. Krauskopf and H. M. Osinga, “Globalizing two-dimensional unstable manifolds of maps,” *International Journal of Bifurcation and Chaos* **8**(3): 483–503, 1998.

[31] D. Li and D. Turaev, “Persistence of heterodimensional cycles,” *Inventiones Mathematicae* **236**(3): 1413–1504, 2024.

[32] H. C. Li, “Numerically computing the stable and unstable manifolds of a three-dimensional map inspired by the Hénon map,” BSc Honours dissertation, Monash University, Melbourne, 2021; available upon request from his supervisor Andy Hammerlindl.

[33] H. E. Lomelí and J. D. Meiss, “Quadratic volume-preserving maps,” *Nonlinearity* **11**(3): 557-574, 1998.

[34] R. Mãné, “A proof of the C^1-stability conjecture,” *Publications Mathématiques de l’Institut des Hautes Études Scientifiques* **66**: 161–210, 1987.

[35] J. D. Meiss, *Differential Dynamical Systems*, Society for Industrial and Applied Mathematics, Philadelphia, PA, 2007.

[36] J. Palis and W. de Melo, *Geometric Theory of Dynamical Systems*, Springer New York, NY, 1982.

[37] J. Palis and S. Smale, “Structural stability theorems,” in S. Smale and S. S. Chern (eds.), *Global Analysis*, Proceedings of Symposia in Pure Mathematics Vol. 14, American Mathematical Society, Providence, RI, 1970, pp. 223–232.

[38] C. Robinson, “Structural stability of C^1-diffeomorphisms,” *Journal of Differential Equations* **22**: 28–73, 1976.

[39] C. Robinson, *Dynamical Systems*, Studies in Advanced Mathematics, 2nd ed., CRC Press, Boca Raton, Fla, 1999.

[40] S. Smale, “Differentiable dynamical systems,” *Bulletin of the American Mathematical Society* **73**: 747–817, 1967.

[41] S. H. Strogatz, *Nonlinear Dynamics and Chaos*, CRC Press, 2nd ed., Boca Raton, FL, 2018.

[42] N. Wong, B. Krauskopf, and H. M. Osinga, “Cascades of heterodimensional cycles via period doubling,” *Communications in Nonlinear Science and Numerical Simulation* **140**: 108328, 2025.

[43] W. Zhang, B. Krauskopf, and V. Kirk, “How to find a codimension-one heteroclinic how to find a codimension-one heteroclinic cycle between two periodic orbits,” *Discrete and Continuous Dynamical Systems* **32**(8): 2825–2851, 2012.